JOURNAL OF AIRCRAFT
Vol. 45, No. 5, September–October 2008

Multidisciplinary Design Exploration for a Winglet

Keizo Takenaka[*] and Keita Hatanaka[†]
Mitsubishi Heavy Industries, Ltd., Nagoya 455-8515 Japan
and
Wataru Yamazaki[‡] and Kazuhiro Nakahashi[§]
Tohoku University, Sendai 980-8579 Japan

DOI: 10.2514/1.33031

In this paper, we describe a multidisciplinary design exploration technique with a high-fidelity analysis applied to the winglet design for a commercial jet aircraft. The minimization of the block fuel at a fixed aircraft operating range and a maximum takeoff weight were selected as design objectives. Both objective functions were estimated from a computational fluid dynamics based aerodynamic drag and a finite element method based structural weight. Various computational fluid dynamics and optimization techniques, such as the midfield drag decomposition method, the automatic computational fluid dynamics mesh generation, the kriging surrogate model, and multi-objective genetic algorithms, were integrated and applied to the detail design exploration. Computational fluid dynamics with the midfield drag decomposition method showed the effect on wave, induced, and profile drag components due to different winglet defining parameters. Practical design decision was explored based on the Pareto front and some design criteria that were uncovered within the numerical optimization. Finally, the design process was validated through the validation of the kriging approximation and aerodynamic characteristics based on the wind-tunnel test.

Nomenclature

a = speed of sound
BF = block fuel
BM = wing-root bending moment
CD = drag coefficient
CD_f = friction drag coefficient
CD_i = induced drag coefficient
CD_p = profile drag coefficient
CD_{sp} = spurious drag coefficient
CD_w = wave drag coefficient
CL = lift coefficient
C_t = tip chord length of wing
C_{wr} = root chord length of winglet
C_{wt} = tip chord length of winglet
$\mathbf{F}_{\mathrm{ind}}$ = induced drag seed vector
$\mathbf{F}_{(\Delta s,\Delta H)}$ = entropy & enthalpy drag seed vector
k_w = form factor of winglet
l_w = span length of winglet
M = Mach number
$\mathbf{n}$ = unit normal vector to a surface
P = pressure
R = gas constant
Re_c = Reynolds number based on mean aerodynamic chord
S_{ref} = reference wing area
S_{wet} = wetted area
t/c = winglet thickness divided by local chord length
$\mathbf{u}$ = velocity vector
V = control volume
W = structural weight
WA = Trefftz plane
γ = specific heat ratio
Δs = entropy variation
ΔH = enthalpy variation
Λ_{w25} = winglet sweep angle at 25% chord length
μ_l = laminar viscosity coefficient
μ_t = turbulent viscosity coefficient
ρ = density

Subscript

∞ = freestream value

I. Introduction

THE winglet has been widely used on commercial aircraft as a means of enhancing fuel efficiency. It also has been widely recognized for its aesthetic value. The winglet, originally designed as an add-on device for existing airplanes, has now become an essential part of aircraft design. The initial concept of the winglet was demonstrated experimentally [1]. A wind tunnel, flight tests, and the database constructed by previous tests have been the main tools for the designers. Then, computational methods, such as the panel method, were used for a more efficient design of the winglet in the early design phase [2]. Most of previous designers focused on induced drag reduction [3] in the early design phase. The effects on the other drag components, that is, profile and wave drag, were mainly confirmed by a wind-tunnel test as the next design step. Also, structural design considerations, such as the weight penalty and flutter characteristics, were considered in the structural design phase in a sequential manner.

Recently, thanks to the advancement of computational fluid dynamics (CFD), computational structural dynamics (CSD), and multidisciplinary design optimization (MDO) techniques, innovative design tools for the designer are available.

The reduction in airplane drag by the winglet is on the order of 10 drag counts (1 drag count $= 1 \times 10^{-4}$), and the incremental drag due to the winglet shape tradeoff is on the order of 1 drag count (about 0.3% of the airplane total drag at cruise). These orders of drag estimation by CFD tend to be unreliable because of the effect of computational mesh dependency. Therefore, accurate drag prediction is essential for the reliable winglet shape design. Another

---

Received 28 June 2007; accepted for publication 30 March 2008.

[*] Research Engineer, Nagoya Aerospace Systems, 10, Oye, Minato-ku, Nagoya. Member AIAA.

[†] Research Engineer, Nagoya Aerospace Systems, 10, Oye, Minato-ku, Nagoya.

[‡] Ph.D. Student, Department of Aerospace Engineering, 6-6-01, Aoba. Student Member AIAA.

[§] Professor, Department of Aerospace Engineering, 6-6-01, Aoba. Associate Fellow AIAA.

difficulty in winglet design is that it includes the variation of each drag component, such as wave, profile, and induced drag. The installation of the winglet will cause induced drag reduction because of the increase in the wing span, the wave drag generation around the wing–winglet junction, and the additional profile drag because of the increase in the wetted area. Therefore, the behavior of each drag component has to be discussed in detail for the advanced winglet design. Recently, as an advanced drag prediction method, the midfield drag decomposition method [4–7] has attracted much attention. In the midfield method, the spurious drag component, which is generated by the spurious entropy production due to numerical diffusion, can be computed and eliminated from the total drag. This enables a more accurate drag prediction. Moreover, the midfield method enables the drag to be decomposed and visualized in the flowfield. By using the midfield method, the total drag can be decomposed into three physical components of wave, profile, and induced drag and one spurious drag component. In Fig. 1, the classification of these drag components is summarized. This advanced analysis approach will achieve a more reliable aerodynamic shape optimization of winglet.

In regard to MDO, these studies of aircraft design have engendered a growing recognition of its importance within industries and universities. As the technology for high-speed wing design (cruise configuration design) has matured, the advancement of aircraft development requires the application of MDO to be superior to competitors. Conventionally, an aircraft outer mold line design proceeds in a sequential manner, that is, aerodynamic design proceeds first with some design requirement from other design processes, such as structures, equipment installation, and manufacturing. Based on this aerodynamics-oriented design process, it is difficult to achieve an optimum design of an aircraft within the usual tight program schedule, whereas MDO is expected to be innovative in the aircraft design process with regards to its multi-objective and simultaneous stand points.

In past MDO research, simple design problems such as airfoil and wing shape design using a high-fidelity CFD tool and complex design problems such as airplane sizing using empirical or analytical tools were quite popular. However, the practical design problem using a high-fidelity tool still has many concerns to overcome.

We have worked to develop high-fidelity MDO systems applicable not only to the conceptual aircraft design phase, but also to the preliminary aircraft design phase in a research and development (R&D) study with Mitsubishi Heavy Industries, Ltd. (MHI) and Tohoku University [8] through the Japanese new commercial jet development program, which is a 5-year research and development project under the auspices of the New Energy and Industrial Technology Development Organization (NEDO) since 2003.[¶]

In the study, we spent considerable effort on MDO techniques of geometry representation, computational mesh modification, optimizers, and the system integration of various complex techniques.

In this paper, we discuss the multidisciplinary design exploration technique with high-fidelity CFD as applied to the winglet design of a commercial jet aircraft for the advanced winglet design. The effectiveness and efficiency of the high-fidelity MDO technologies to the practical aircraft design is discussed.

II. Design Process and Applied Technologies

A. Design Problem Definition and Overview of the Design Process

In the present study, we conducted winglet design for the wing–body configuration of a commercial jet. The minimization of the block fuel derived from the aerodynamic drag and structural weight was selected as an objective function. The block fuel is defined as the minimum fuel mass for a fixed range. In addition, the minimization of the maximum takeoff weight (MTOW), which is related to the airport landing fee charged in some airports for commercial jets, was considered as another objective function.

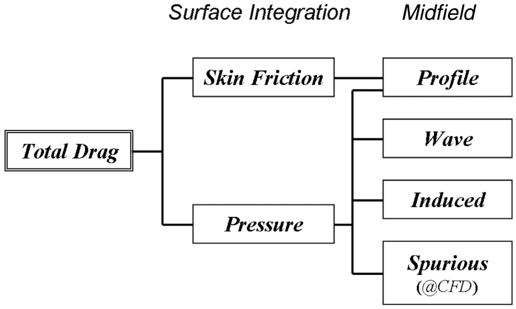

Fig. 1 Drag components.

There are many optimizers, such as genetic algorithms [9], the adjoint method [10] and the kriging surrogate model based optimization [11]. The authors have considerable experience with a wide variety of optimizers and concluded that the kriging model method was most suitable for the present study because kriging model based optimization is very efficient for a design problem with multiple objectives and a small number of design variables.

A wide variety of techniques was applied to the present design optimization. Figure 2 shows the flowchart of the design process.

First, sample individuals (winglets) were selected from the design space. The method used to scatter points uniformly in the space is called "space filling." In this study, Latin hypercube sampling (LHS) [12] was used for the space filling. This method ensures that a point always exists inside the interval partitioned by the number of sample points. A total of 32 sample individuals were selected from the initial search region. Figure 3 shows the initial sample individuals. A wide variety of winglet shapes were considered in the design.

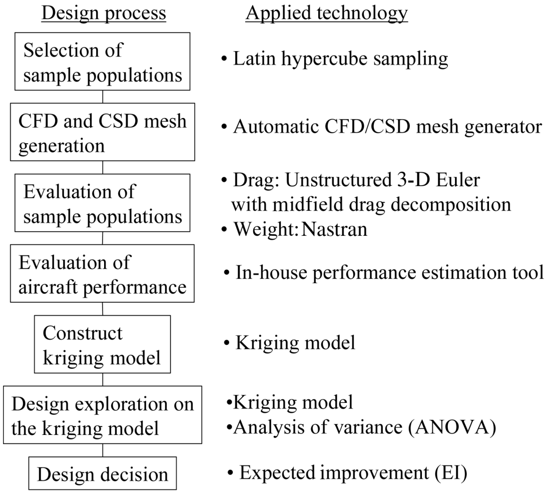

Fig. 2 Design flowchart.

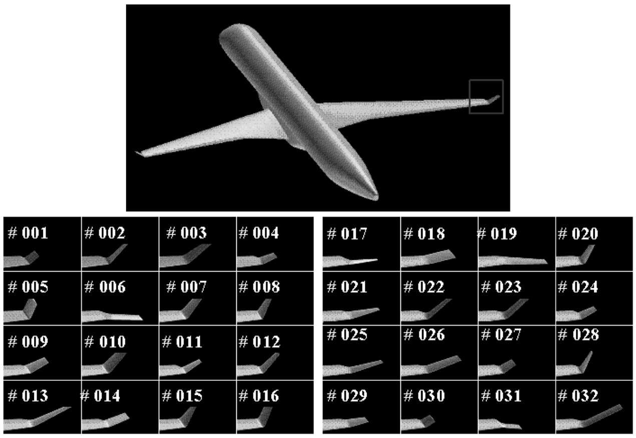

Fig. 3 Winglet shape of sample individuals (backward view).

[¶] Data available online at http://www.nedo.go.jp/english/index.html [retrieved 28 June 2008].

An unstructured Euler CFD analysis at Mach 0.80, 1 g cruise CL was conducted for each winglet shape. Navier–Sokes simulations are still expensive for three-dimensional design problems. Therefore, we chose Euler CFD for the design exploration and conducted a validation by Navier–Stokes analysis for the designed configurations. Euler CFD with the drag decomposition method has been successfully applied to the transonic drag evaluation in the past research [13–15]. However, the Euler CFD cannot capture the behavior of profile drag. An additional wetted area due to the installation of the winglet will lead to additional profile drag. In this study, the profile drag was taken into account by a simple algebraic model and added to the inviscid drag.

From the CFD results, wave drag (CD_w) and induced drag (CD_i) were extracted using the midfield drag decomposition technique. As for profile drag (CD_p), the increase in the profile drag due to the additional wetted area of the winglet was estimated with the following simple algebraic model**:

$$\begin{aligned}\Delta CD_p &= k_w \cdot \Delta CD_f\\ \Delta CD_f &= \left[\frac{0.455}{(\log_{10} Re_c)^{2.58}}(1+0.15M_\infty^2)^{-0.58}\right]\frac{\Delta S_{\text{wet}}}{S_{\text{ref}}}\\ k_w &= 1+\frac{2C_w(t/c)\cos^2\Lambda_{w25}}{\sqrt{1-M_\infty^2\cos^2\Lambda_{w25}}}\\ &\quad+\frac{C_w^2\cos^2\Lambda_{w25}(t/c)^2(1+5\cos^2\Lambda_{w25})}{2(1-M_\infty^2\cos^2\Lambda_{w25})}\end{aligned} \tag{1}$$

where $C_w = 1.1$. ΔS_{wet}, and Λ_{w25} are the additional wetted area and sweep angle at 25% chord of the winglet, respectively.

Also, the structural weight penalty of the wing box due to winglet installation was estimated by MSC Nastran††. Structural optimization of the wing box was performed to achieve the minimum weight within the constraints of the strength requirements. For the strength evaluation, the static load was calculated from the pressure distribution on the wing and winglet, which is computed by the Euler solver.

Then, the block fuel and maximum takeoff weight were evaluated by an in-house performance analysis tool. In this module, the wing box weight and aerodynamic drag were used as input. In the tool, the drag was evaluated by the following formula:

$$CD = CD_p + CD_i + CD_w \tag{2}$$

ΔCD_p, ΔCD_i, and ΔCD_w as derived from the drag evaluation were added to the baseline (no winglet) drag, and the structural weight penalty ΔW was also added to the baseline weight. Then, the block fuel was estimated.

The maximum takeoff weight was estimated using the fuel carried derived from the block fuel and structural weight.

Finally, the design exploration and design decision were conducted using data mining techniques.

In the present study, we used the kriging model, the function analysis of variance (ANOVA) [16], and the expected improvement (EI) [17].

In the entire design process shown in Fig. 2, the bottleneck is the CFD computations. However, thanks to parallel CFD computations, the design completed within a day.

A brief introduction to each technology adopted in the present study is presented in the following sections.

B. Geometry Definition

As the baseline geometry, the wing–body configuration of a commercial jet aircraft was used. The winglet shape was defined by six variables as shown in Fig. 4. The upper and lower limits of each design variable were defined by the statistical survey of existing aircraft. The upper limit of the winglet cant angle is 84 deg, which means a simple wing extension for the baseline wing with a 6 deg dihedral.

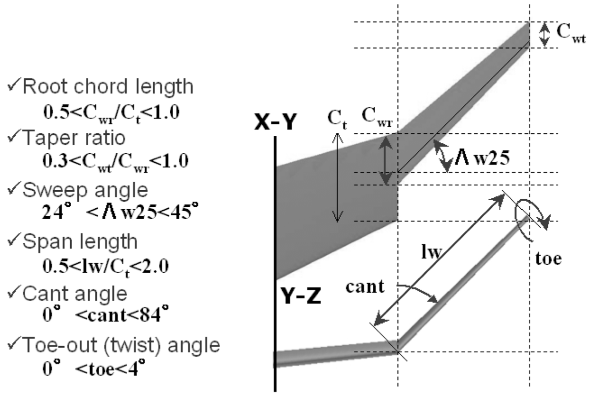

Fig. 4 Winglet shape definition.

The airfoil section of the winglet was defined as the modification of the wing tip section with the rule t/c constant. At the wing-winglet junction, a tangential smooth connection was achieved using a Bezier curve, as shown in Fig. 5.

C. CFD Solver and Mesh

For the CFD solver, we used the Tohoku University Aerodynamic Simulation (TAS) unstructured Euler code. The compressible Euler equations were solved with a finite volume cell-vertex scheme. The numerical flux was computed using the Harten–Lax–van Leer–Einfields–Wada (HLLEW) approximate Riemann solver [18]. Second-order spatial accuracy was achieved with a linear reconstruction of the primitive gas dynamic variables inside the control volume with Venkatakrishnan's limiter [19]. The lower-upper symmetric Gauss–Seidel (LU-SGS) implicit method for unstructured meshes was used for the time integration [20].

The TAS code is fully vectorized with an edge-coloring technique [20] and parallelized with a message passing interface (MPI) and domain partitioning technique [21].

The computational mesh for the TAS code was generated automatically with the following steps.

1) The background mesh of body is prepared by stereo-type lithography (STL) [22] and the wing with winglet is prepared by PLOT3D format.

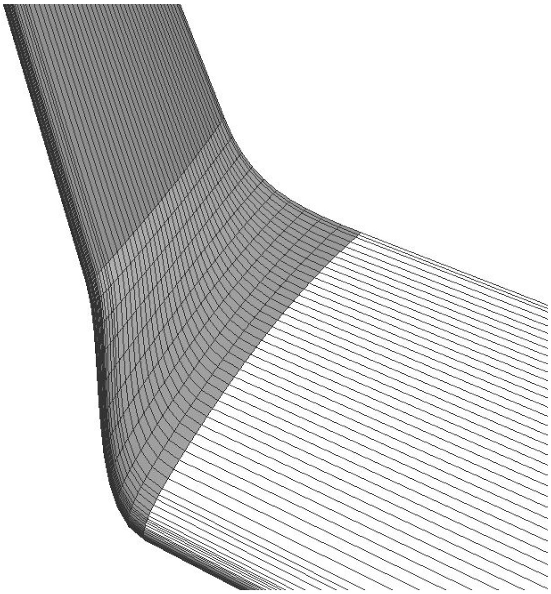

Fig. 5 Enlarged view of wing-winglet junction.

**Data available online at http://www.mscsoftware.com/products/msc_nastran.cfm?Q=131&Z=396&Y=422 [retrieved 14 July 2008].

††Data available online at http://www.mscsoftware.com [retrieved 30 June 2008].

2) The junction line between the body and wing is extracted and other geometric characteristic lines are also extracted automatically.
3) The node distributions are specified along the extracted characteristic lines.
4) Unstructured surface meshes are generated using the advancing front method of TAS–mesh [23].
5) Unstructured volume meshes are generated using Delaunay tetrahedral meshing [23].

The aforementioned mesh generation process enables us to generate a computational mesh around complex geometries including geometric junctions with robustness and efficiency.

In the present design optimization, the CFD mesh of each winglet configuration was generated with the predefined identical node distributions along the extracted characteristic lines, which means that each CFD mesh including surface and volume has an almost identical mesh density. As for the efficiency, it took only about 5 min for each mesh generation.

Such a highly reproducible mesh generation process greatly contributed to a reduction in the numerical error as well as to the drag decomposition method.

The number of nodes using unstructured mesh was about 500,000 in the current study. The CFD computation in this study was executed by a master–slave-type parallel computation using NEC SX-7 of the Supercomputing System Information Synergy Center at Tohoku University. The 32 samples were evaluated by 32 CPUs in one execution, which took only 2 h.

D. Midfield Drag Decomposition Method

To extract the drag from the calculated CFD results, the midfield drag decomposition method (hereafter called the near-field method) was applied instead of wall boundary surface integration for an accurate estimation and detailed investigation. By using the drag decomposition method, an accurate drag prediction can be achieved by excluding the effect of unphysical entropy production. This has been validated coupled with the TAS code for transonic flow in the author's previous works [6,7].

The midfield method is derived from the far-field method by applying the divergence theorem. By using the divergence theorem, the entropy and enthalpy term of the far-field method can be transformed as follows:

$$CD_{(\Delta s,\Delta H)} = \iint_{WA} \mathbf{F}_{(\Delta s,\Delta H)} \cdot \mathbf{n} \mathrm{d}s \cong \iint_{V}\int \nabla\cdot\mathbf{F}_{(\Delta s,\Delta H)}\,\mathrm{d}v \tag{3}$$

where WA is the Trefftz plane and V is the flowfield around the aircraft.

$\mathbf{F}_{(\Delta s,\Delta H)}$ is the entropy and enthalpy drag seed vector:

$$\mathbf{F}_{(\Delta s,\Delta H)} = -\rho\Delta\bar{u}\mathbf{u}/qS_{\mathrm{ref}} \tag{4}$$

$\Delta\bar{u}$ of Eq. (4) can be expressed in Taylor's series as follows:

$$\begin{aligned}\Delta\bar{u}/u_\infty &= f_{s1}(\Delta s/R) + f_{s2}(\Delta s/R)^2 + f_{H1}(\Delta H/u_\infty^2)\\ &\quad + f_{H2}(\Delta H/u_\infty^2)^2 + f_{sH2}(\Delta s/R)(\Delta H/u_\infty^2) + O(\Delta^3)\end{aligned} \tag{5}$$

Here,

$$f_{s1} = -\frac{1}{\gamma M_\infty^2}, \qquad f_{s2} = -\frac{1+(\gamma-1)M_\infty^2}{2\gamma^2 M_\infty^4}, \cdots \tag{6}$$

In the work, we adopt only first- and second-order entropy variation terms.

The drag decomposition of the entropy drag term is derived from the domain decomposition of the flowfield. Then Eq. (3) can be transformed as follows:

$$\begin{aligned}CD_{(\Delta s,\Delta H)} &= \iint_{V\mathrm{shock}}\int \nabla\cdot\mathbf{F}_{(\Delta s,\Delta H)}\,\mathrm{d}v + \iint_{V\mathrm{profile}}\int \nabla\cdot\mathbf{F}_{(\Delta s,\Delta H)}\,\mathrm{d}v\\ &\quad + \iint_{V\mathrm{spurious}}\int \nabla\cdot\mathbf{F}_{(\Delta s,\Delta H)}\,\mathrm{d}v = CD_w + CD_p + CD_{\mathrm{sp}}\end{aligned} \tag{7}$$

The advantage of the midfield method is that it can divide the entropy drag into the wave, profile, and spurious drag components, and allow visualization of the generated positions and the strength of the drag in the flowfield. The domain decomposition of the flowfield is based on the following shock and profile detective functions. For the detection of the shock region, the following function is used:

$$f_{\mathrm{shock}} = (\mathbf{u}\cdot\nabla P)/(a|\nabla P|) \tag{8}$$

For the detection of the wake and boundary-layer region, the following function is used:

$$f_{\mathrm{profile}} = (\mu_l + \mu_t)/(\mu_l) \tag{9}$$

The regions that satisfy $f_{\mathrm{shock}} \geq 1$ and $f_{\mathrm{profile}} \geq C\cdot(f_{\mathrm{profile}})_\infty$ are recognized as the upstream region of shock waves and the profile region, respectively. C is a cutoff value for selecting the profile region, and $C = 1.1$ was used in this study.

Likewise, the induced drag can be evaluated as follows:

$$CD_i = \iint_{WA} \mathbf{F}_{\mathrm{ind}}\cdot\mathbf{n}\,\mathrm{d}S \cong \iint_{\infty} \mathbf{F}_{\mathrm{ind}}\cdot\mathbf{n}\,\mathrm{d}S \tag{10}$$

Here,

$$\begin{aligned}\mathbf{F}_{\mathrm{ind}}\cdot qS_{\mathrm{ref}} = \Big(&(\rho_\infty/2)[(u_y^2+u_z^2) - (1-M_\infty^2)(\Delta u_x)^2],\\ &-\rho_\infty u_y \Delta u_x, \qquad -\rho_\infty u_z \Delta u_x \Big)\end{aligned} \tag{11}$$

E. Structural Weight Estimation

Structural optimization of a wing box was performed to achieve the minimum weight (minimize thickness of shell elements) with the constraints of strength requirements. Given the wing and winglet aeroline for each individual, the finite element model of the wing box and winglet was generated automatically by an in-house finite element method (FEM) generator for the structural optimization. Figure 6 shows a schematic view of the FEM model. The wing box model mainly consists of shell elements representing the skin, spar, and rib. Other wing components, such as control surfaces and subsystems, are modeled using concentrated mass elements. Load transmission from the winglet to the wing box was simulated with a rigid bar model. The winglet weight was considered as the volume of a winglet multiplied by the equivalent density of an existing winglet structure.

In the present structural optimization, the strength is evaluated using MSC Nastran. For the strength evaluation, the static load is calculated from the pressure distribution on the wing and winglet, which is computed by the Euler solver, assuming an up-gust

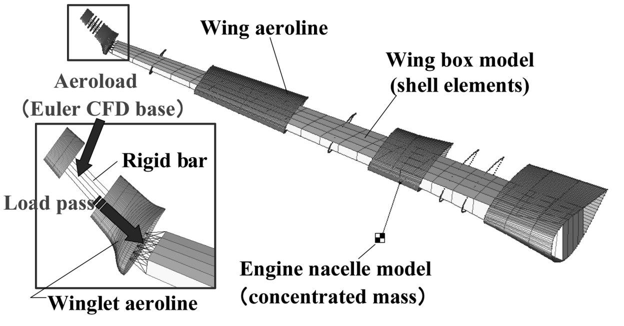

Fig. 6 Schematic view of the FEM model for the wing with winglet configuration.

condition. Then, a static analysis is conducted to obtain the stress on each element of the wing box. For the load and stress analysis in the actual aircraft development phase, there are many evaluation conditions (maneuver load, gust load, etc.). However, in the present study, as is well known, the weight penalty is almost proportional to the wing-root bending moment, as will be shown in the following section. Therefore, such single point evaluation seemed enough for the derivation of the weight sensitivity to the wing-root bending moment change.

The present structural optimization is based on the following optimality criteria:

$$\sigma_i / F_i = \mathrm{const} \tag{12}$$

where σ denotes the stress for the ith shell element of the wing box and F_i is the allowable stress.

In the structural optimization, the thickness of the shell elements is resized iteratively until the weight change converges sufficiently under the strength constraints.

The resizing formula is as follows:

$$t_i^{\mathrm{new}} = \frac{t_i^{\mathrm{old}}}{(\gamma_{\min})_i} \tag{13}$$

where $\gamma_{\min}$ denotes the minimum strength factor and the strength constraints are considered as follows:

$$\begin{bmatrix} \sigma_{\mathrm{compressive}} \\ \sigma_{\mathrm{tensile}} \\ \sigma_{\mathrm{shear}} \end{bmatrix} < F \tag{14}$$

$$t_i > t_{\min} \tag{15}$$

F. Kriging Model

The kriging model is a method of response surface model (RSM) that predicts unknown values from data observed at known locations. It minimizes the error of the predicted values, which are estimated by the spatial distribution of the predicted values.

The kriging model expresses the unknown function $y(\mathbf{x})$ as

$$y(\mathbf{x}) = \mu + Z(\mathbf{x}) \tag{16}$$

where $\mathbf{x}$ is an m-dimensional vector (m-design variables), μ is a constant global model, and $Z(\mathbf{x})$ represents a local deviation at an unknown point $\mathbf{x}$ expressed using the stochastic process. The sample points are interpolated using the Gaussian random function as the correlation function to estimate the trend of the stochastic processes. In the kriging model, a special weighted distance is used instead. The distance function between the point at $\mathbf{x}^i$ and $\mathbf{x}^j$ is expressed as

$$d(\mathbf{x}^i, \mathbf{x}^j) = \sum_{k=1}^{m} \theta_k |\mathbf{x}_k^i - \mathbf{x}_k^j|^2 \tag{17}$$

where $\theta_k (0 \leq \theta_k \leq \infty)$ is the kth element of the correlation vector parameter θ.

By using the special weighted distance and the Gaussian random function, the correlation between the point $\mathbf{x}^i$ and $\mathbf{x}^j$ is defined as

$$\mathrm{Corr}\,[Z(\mathbf{x}^i), Z(\mathbf{x}^j)] = \exp[-d(\mathbf{x}^i, \mathbf{x}^j)] \tag{18}$$

The kriging predictor is

$$\hat{y}(\mathbf{x}) = \hat{\mu} + \mathbf{r}' R^{-1} (\mathbf{y} - \mu \mathbf{I}) \tag{19}$$

where $\hat{\mu}$ is the estimated value of μ, R denotes the $n \times n$ matrix, whose (i, j) element is $\mathrm{Corr}[Z(\mathbf{x}^i), Z(\mathbf{x}^j)]$. $\mathbf{r}$ is a vector whose ith element is

$$r_i(x) \equiv \mathrm{Corr}[Z(\mathbf{x}), Z(\mathbf{x}^i)] \tag{20}$$

$\mathbf{y} = [y(x^1), \cdots\cdots, y(x^n)]$ and $\mathbf{I}$ denote an m-dimensional unit vector.

The detailed derivation of Eq. (18) can be found in [24].

The unknown parameter to be estimated for constructing the kriging model is $\boldsymbol{\theta}$. This parameter can maximize the following likelihood function:

$$Ln(\hat{\mu}, \hat{\sigma}^2, \boldsymbol{\theta}) = -\frac{n}{2} \ln(2\pi) - \frac{n}{2} \ln(\hat{\sigma}^2) - \frac{n}{2} \ln(|R|) - \frac{1}{2\hat{\sigma}^2} (\mathbf{y} - \mathbf{I}\hat{\mu}) R^{-1} (\mathbf{y} - \mathbf{I}\hat{\mu}) \tag{21}$$

G. Function Analysis of Variance

To identify the effect of each design variable on the objective functions, the total variance of the model is decomposed into the variance component due to each design variable. This is called the functional analysis of variance. The decomposition is accomplished by integrating the variables out of the model $\hat{y}$.

The total mean ($\hat{\mu}_{\mathrm{total}}$) and variance ($\hat{\sigma}^2_{\mathrm{total}}$) of model $\hat{y}$ are as follows:

$$\hat{\mu}_{\mathrm{total}} = \int \cdots \int \hat{y}(x_1, \ldots, x_n)\, \mathrm{d}x_1 \cdots \mathrm{d}x_n \tag{22}$$

$$\hat{\sigma}^2_{\mathrm{total}} = \int \cdots \int [\hat{y}(x_1, \ldots, x_n) - \hat{\mu}]^2\, \mathrm{d}x_1 \cdots \mathrm{d}x_n \tag{23}$$

The main effect of variable x_i is

$$\mu_i(x_i) = \int \cdots \int \hat{y}(x_1, \ldots, x_n)\, \mathrm{d}x_1 \cdots \mathrm{d}x_{i-1}\, \mathrm{d}x_{i+1} \cdots \mathrm{d}x_n - \hat{\mu} \tag{24}$$

The two-way interaction of variance x_i and x_j is

$$\begin{aligned} \mu_{i,j}(x_i, x_j) &= \int \cdots \int \hat{y}(x_1, \ldots, x_n)\, \mathrm{d}x_1 \cdots \mathrm{d}x_{i-1}\, \mathrm{d}x_{i+1} \cdots \mathrm{d}x_{j-1}\, \mathrm{d}x_{j+1} \cdots \mathrm{d}x_n \\ &\quad - \hat{\mu}_i(x_i) - \hat{\mu}_j(x_j) - \hat{\mu} \end{aligned} \tag{25}$$

The variance due to the design variable x_i is

$$\int [\mu_i(x_i)]^2\, \mathrm{d}x_i \tag{26}$$

The proportion of the variance due to design variable x_i of the total variance of model can be expressed by dividing Eq. (26) by Eq. (24):

$$\frac{\int [\mu_i(x_i)]^2}{\int \cdots \int [\hat{y}(x_1, \ldots, x_n) - \hat{\mu}]^2\, \mathrm{d}x_1 \cdots \mathrm{d}x_n} \tag{27}$$

This value indicates the sensitivity of the model to the variation of each design variable.

H. Expected Improvement

To find the global optimum in the kriging model, both the estimated function value and the uncertainty at the unknown point are considered at the same time. Based on these values, the point having the largest probability of being the global optimum is found. The probability of being the global optimum is expressed by the criterion EI. The EI in a minimization problem is expressed as follows:

$$E(I) = s \int_{-\infty}^{f^n_{\min}} (f_{\min} - z) \phi(z)\, \mathrm{d}z \tag{28}$$

where $f^n_{\min} = (y_{\min} - \hat{y})/s$, $z = (y - \hat{y})/s$ and

$$I(\mathbf{x}) = \begin{cases} [y_{\min} - y(\mathbf{x})] & \text{if } y(\mathbf{x}) < y_{\min} \\ 0 & \text{otherwise} \end{cases} \tag{29}$$

III. Multidisciplinary Design Exploration

A. Aerodynamic Effects of a Winglet

From the CFD analysis of 32 sample individuals, the detailed aerodynamic effects of winglet were extracted. The incremental value for the baseline wing body (no winglet) was evaluated, so that Δ hereafter denotes the increment from the baseline.

Obviously, the most dominant variable for drag reduction was the winglet span length, and the most dominant drag component contributing to drag reduction was induced drag. Figure 7 shows the winglet span length effects on drag and Fig. 8 shows the winglet span length effect on induced drag. In both figures, each dot shows each population of 32 individuals, and the line is fit by the linear least-squares method. The standard deviation and maximum deviation from the fitted line are shown in these figures. The winglet span length is linearly correlated with induced drag reduction and total drag reduction. However, these deviations from the least-squares line are not negligible, which implies contributions from other design variables.

Also, as shown in Fig. 9, the wing-root bending moment increase is linearly related to drag reduction, which shows the tradeoff between the aerodynamic performance and weight penalty.

To obtain detailed understanding of the aerodynamic effects of other variables, the kriging model was used for a function approximation. The dominant variable in the objective function is fixed, and the other variable effects on the kriging model are investigated. LHS was used for sampling in the kriging model.

Figure 10 shows the winglet cant angle effects on wave drag.

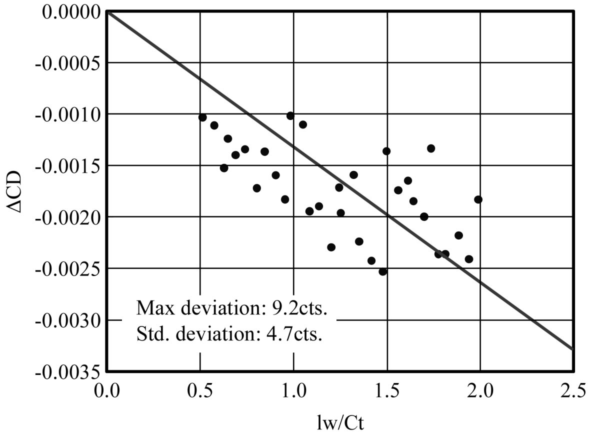

Fig. 7 Winglet span length effect on drag.

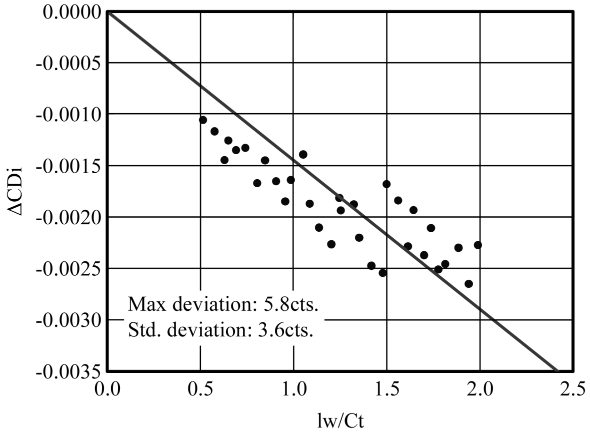

Fig. 8 Winglet span length effect on induced drag.

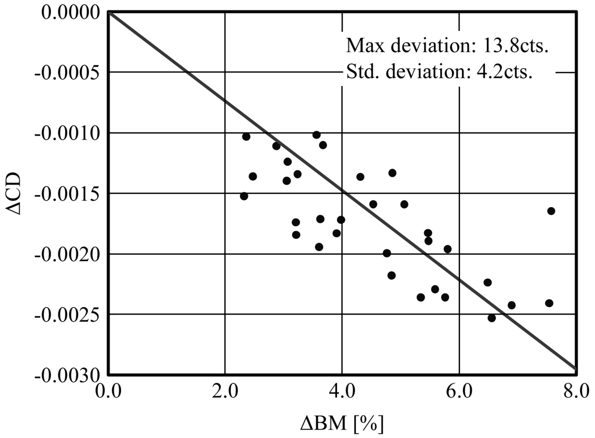

Fig. 9 Relationship between drag and wing-root bending moment.

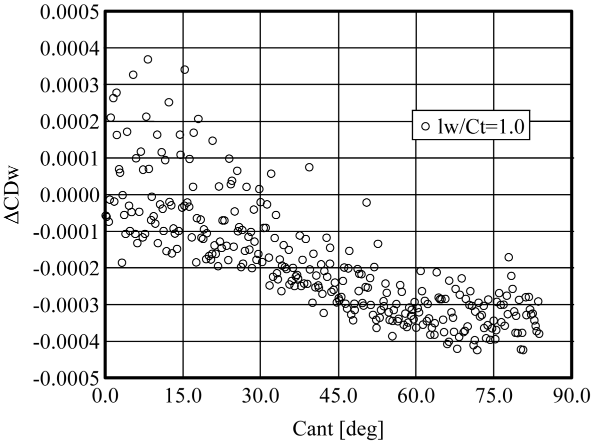

Fig. 10 Cant angle effect on wave drag with fixed winglet span length.

For wave drag reduction, as the cant angle increases, the wave drag decreases. Two reasons are responsible for this effect. One reason is the aerodynamic load relief of the wing excluding the winglet due to the winglet as a lifting surface. As the cant angle increases, the lift of the winglet increases. Therefore, the lift dependent wave drag of the wing itself decreases as the cant angle increases at a constant lift. The other reason is the shock wave generation around the wing–winglet junction area due to the aerodynamic interference. When the cant angle is small, the flow around the junction area is accelerated due to the contraction of the stream tube around the junction area; such

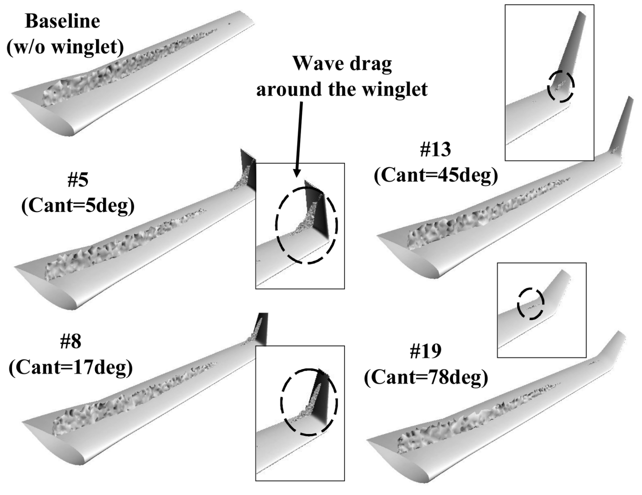

Fig. 11 Wave drag visualization ($F_{\text{shock}} > 1$) as a function of cant angle.

accelerated flow leads to the shock wave generation. Figure 11 shows wave drag visualization as a function of the cant angle, and Fig. 12 shows the contributions of the wing and winglet to the wave drag at constant *CL*. The region where $F_{\mathrm{shock}} > 1$ is shown in Fig. 11. The two effects are clearly observed in both figures.

Figure 13 shows the winglet cant angle effects on the wave drag and wing-root bending moment.

For the wing bending moment, as the cant angle increases, the wing-root bending moment increases and the sensitivity of the bending moment to the cant angle increases as the winglet span length increases. That's why the small cant angle and small winglet span of the classical retrofit-type winglet is advantageous, that is, to minimize the need for reinforcement treatment of the wing structure.

Then, to identify the effect of each design variable in the objective function at a glance, the ANOVA is performed. The design variables and their interactions (covariance) including their proportion to the total variance is shown in Figs. 14–17.

From these figures, we can draw the following conclusions regarding the winglet design:

1) For drag reduction, the winglet span length and cant angle are the dominant parameters

2) The winglet span is dominant in induced drag, whereas the cant angle is dominant in wave drag.

3) For wave drag reduction, the covariance is significant, which requires good tailoring of all parameters.

4) For the wing-root bending moment, the winglet span and cant angle are still dominant; however, the sensitivity of other parameters are larger compared with the drag.

B. Weight and Aircraft Performance Analysis

Structural optimization for 32 points was conducted, and the structural wing box weight was estimated. Figure 18 shows the

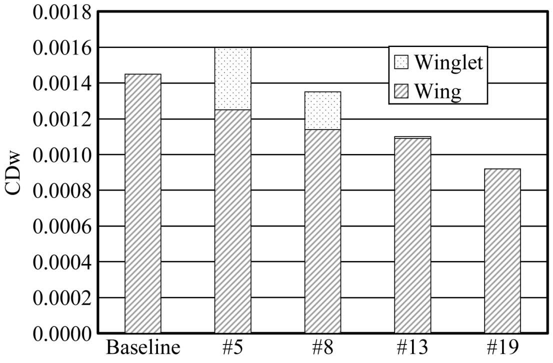

Fig. 12 Wave drag of wing and winglet for each sample at a constant *CL*.

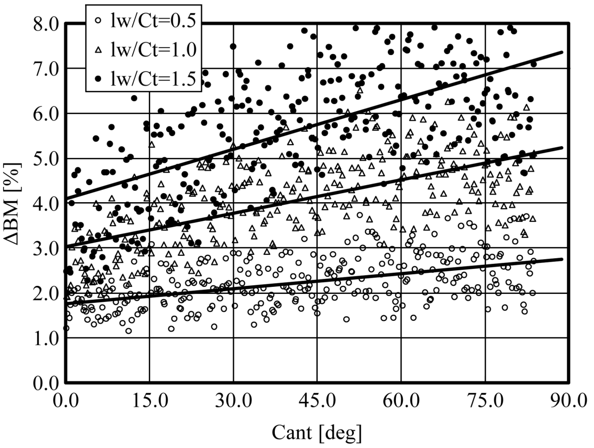

Fig. 13 Cant angle effect on wing-root bending moment with fixed winglet span length.

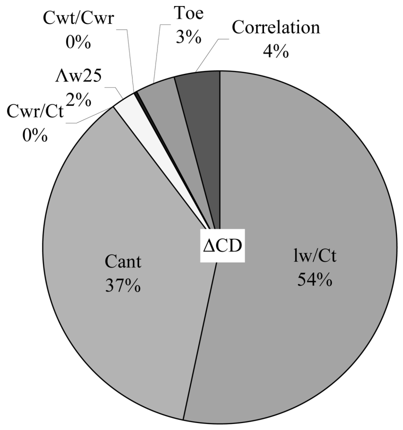

Fig. 14 ANOVA results for drag.

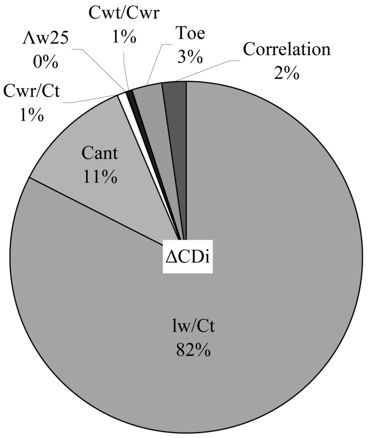

Fig. 15 ANOVA results for induced drag.

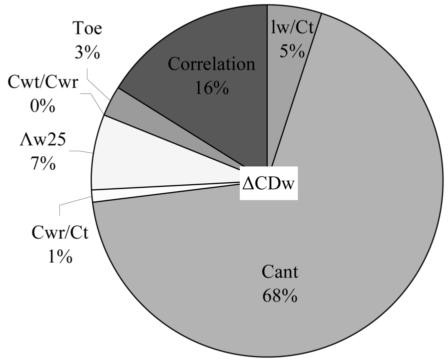

Fig. 16 ANOVA results for wave drag.

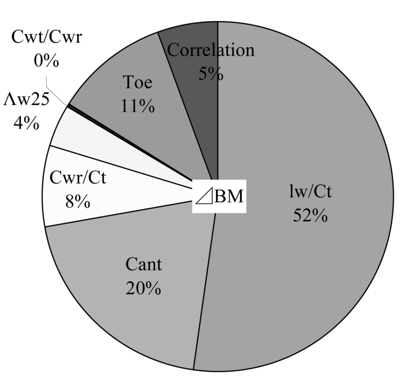

Fig. 17 ANOVA results for wing-root bending moment.

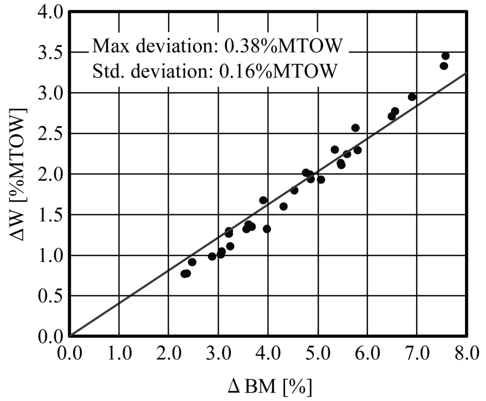

Fig. 18 Relationship between wing box weight and wing-root bending moment.

relationship between the wing box weight and wing-root bending moment. As was expected, the structural weight has a strong linear dependence on the wing-root bending moment in this design problem.

Then, aircraft performance was estimated from the obtained drag and weight data. Figure 19 shows the estimated performance chart. The figure shows the wing box weight, drag, block fuel, and MTOW. In the figure, the wing box weight was divided by the MTOW of the baseline. The block fuel reduction due to the winglet in the current design space is 2–5%. The structural weight penalty is 0.5–3.5%, whereas the MTOW increase is within 2%, which is because fuel carried decreases due to block fuel improvement.

For the next step, the kriging model was constructed for block fuel and MTOW as a function of 32 sample points. Then, the Pareto front was derived through the minimization of both objectives in the kriging model by a multi-objective genetic algorithm (MOGA) [9].

Figure 20 shows the estimated Pareto front. As seen in the figure, there is a tradeoff between the block fuel improvement and MTOW reduction.

Figures 21 and 22 show the effect on the block fuel in the Pareto front of the winglet span length and cant angle, respectively. From both figures, it can be seen that block fuel improves as the span length and cant angle increase. Especially, the cant angle in the Pareto front becomes significant at values, which means a simple wing extension seems to be efficient for the current design problem. In other words, the drag reduction excels the MTOW increase for the current design problem.

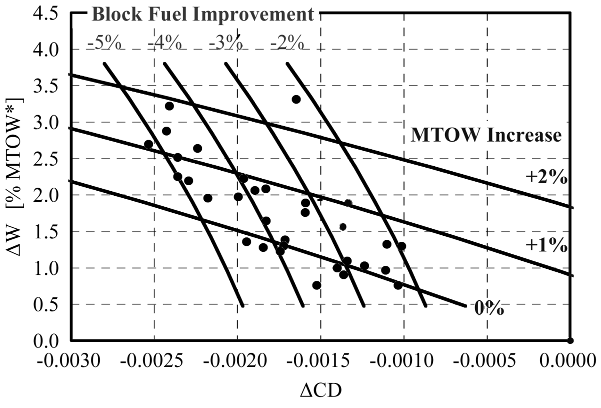

Fig. 19 Estimated aircraft performance chart.

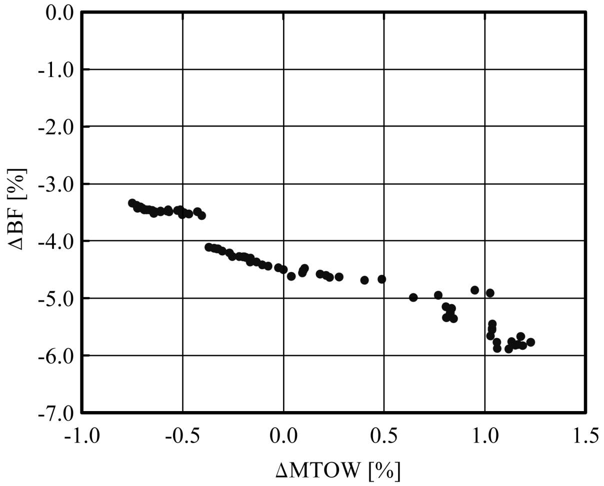

Fig. 20 Estimated Pareto front.

C. Design Decision

From the detailed investigations so far, the final candidate for the winglet shape was decided. Past researchers had derived the Pareto front or sensitivity information for MDO problems. However, the design decision is not so straightforward that a single candidate can be clearly chosen from the obtained Pareto front. Many factors affect the decision in the practical design situation. It is very natural that all factors that affect the decision cannot always be covered with numerical optimizations. In the present study, low-speed aerodynamic characteristics, flutter characteristics, and the aesthetic standpoint were not covered. Therefore, design decisions should be coupled with MDO results for such uncovered information. The present design process based on kriging approximation is very capable for such a point of view compared with other optimization algorithms, such as gradient base optimization. The present process is developed to reveal the whole structure of the design space using

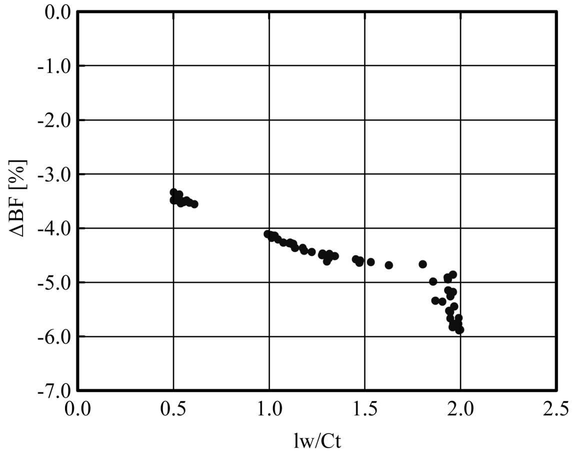

Fig. 21 Winglet span length effect on the block fuel in the Pareto front.

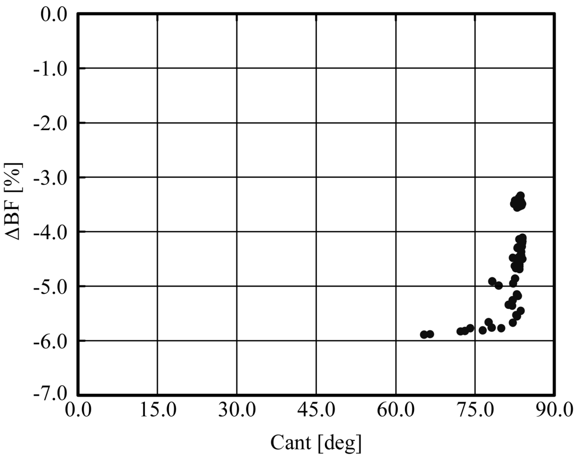

Fig. 22 Winglet cant angle effect on the block fuel in the Pareto front.

various sensitivities and tradeoff information, not to give optimal solutions. Therefore, it is flexible enough to handle the uncovered information.

In the present study, EI is used for the decision. The EI maximization on the kriging model was conducted by MOGA. Figure 23 shows examples of normalized EI distributions for the block fuel and MTOW as a function of the design variables, where an EI value of 1 means most probable for the minimization of the objective function. In the figure, for the sweep angle, there are some optimum values for both objective functions around 35 deg. For the winglet span length, there is a clear tradeoff between the two objective functions. For the winglet taper ratio, both objective functions do not have clear dependency.

The decision was made from the EI and some additional criteria for uncovered design consideration.

Of course, the criteria depend on the strategy of the designers. Examples of the decision criteria for the present study are as follows: 1) smaller cant is a lower risk for low-speed stall and buffet characteristics, 2) larger toe-out angle is a lower risk for flutter characteristics, 3) smaller taper ratio and moderate cant angle are better from the aesthetic standpoint, 4) landing fee dependence on MTOW should be equal to the category of the baseline, and 4) the difference from the Pareto front should be minimized.

We determined each design variable so as to maximize the EI as much as possible, considering the tradeoff between the Pareto front and the aforementioned criteria. As a result, one candidate was selected (hereafter referred to as the "designed" winglet). Also, one winglet, which has a smaller cant and larger chord length than those of the designed winglet as the representative of the conventional winglet, was selected for comparative use (hereafter referred to as the "conventional" winglet). Figure 24 shows the designed winglet configuration and Fig. 25 shows the conventional one.

Figure 26 shows the comparison of the block fuel and MTOW of the designed winglet, the conventional winglet, and the Pareto front. From the figure, the designed winglet configuration has an almost equivalent performance as the Pareto front, whereas the conventional one has no MTOW penalty and a 1% block fuel deterioration as compared with the Pareto front.

IV. Validation

A. Validation of the Kriging Approximation

In the present study, the validity of the design depends on the accuracy of the drag estimation, weight estimation, and kriging model approximation. As for the kriging model, one of the advantages is its ability to control the accuracy of the approximation. If necessary, the accuracy of the approximation is easily augmented by using additional samples of some criteria, such as the EI maximization of an objective function.

To validate the approximation, a comparison of aerodynamic characteristics between the approximations and Euler CFD results for two selected winglets was conducted. Table 1 shows the result of this comparison. The result was sufficient. The difference was 1 drag count and 0.1% for the wing-root bending moment.

Therefore, we found that 32 sample points were enough for the present study.

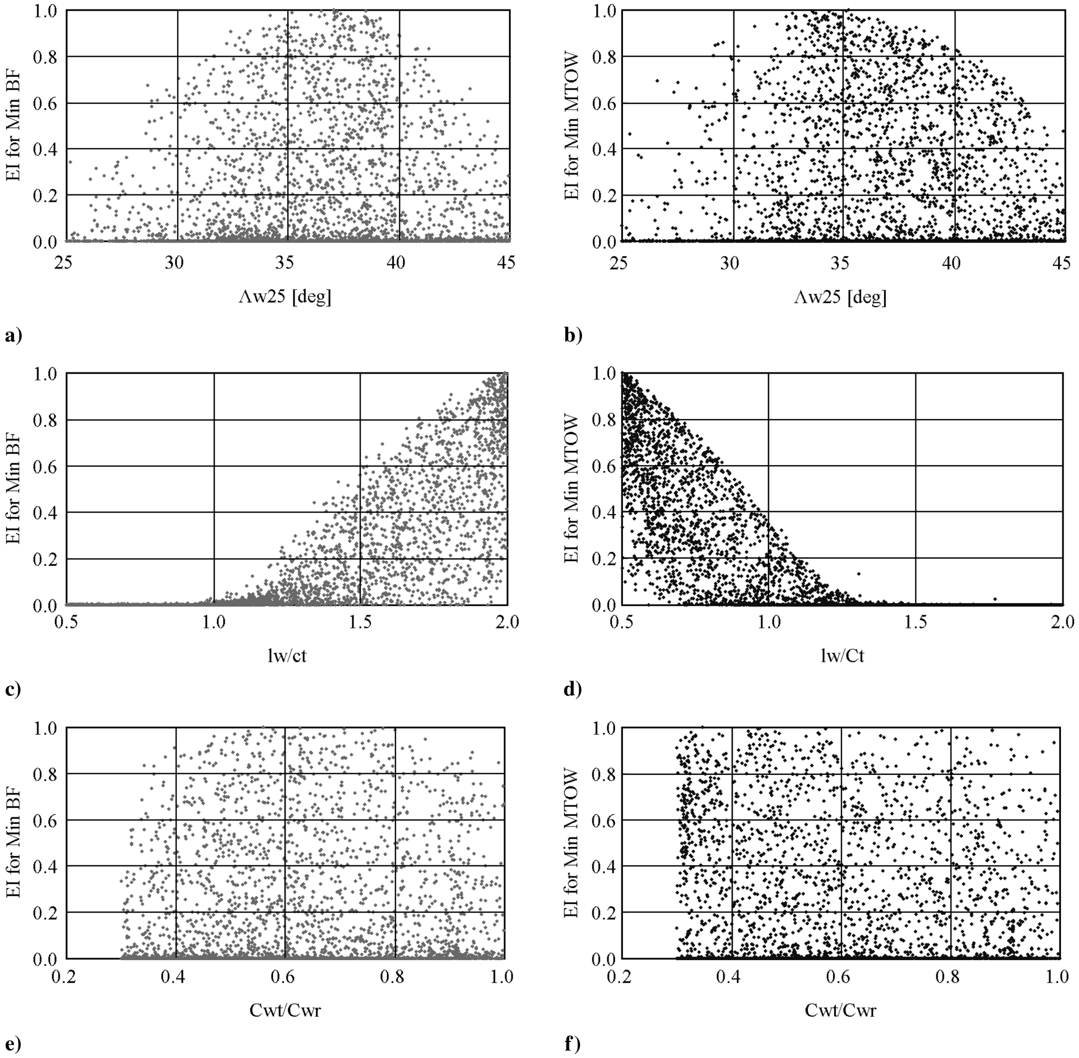

Fig. 23 Normalized EI for block fuel and MTOW as a function of the design variables.

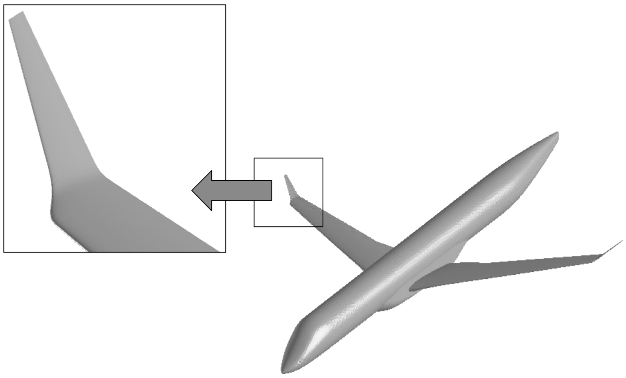

Fig. 24 Designed winglet configuration.

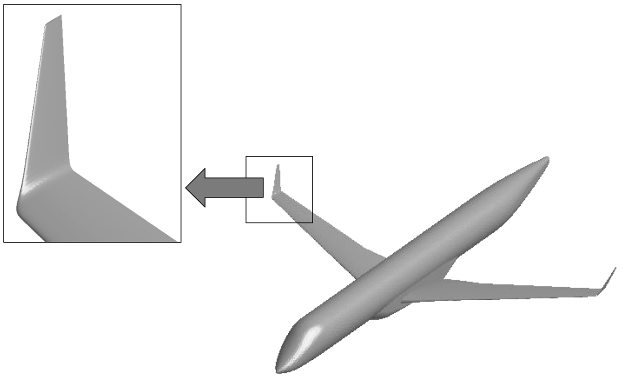

Fig. 25 Conventional winglet configuration.

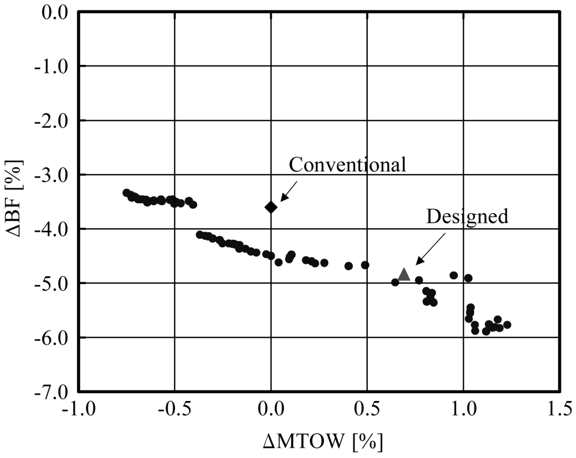

Fig. 26 Comparison of selected configurations and Pareto front.

B. Validation of the Aerodynamics Design by Wind-Tunnel Test

To validate the aerodynamic design of the winglet, a wind-tunnel test was conducted as a part of a preliminary development wind-tunnel test. The wind tunnel used was the JAXA 2 m × 2 m continuous transonic wind tunnel[‡‡] in Japan. The model we used was a 3.4% scale model and had a Reynolds number based on a mean aerodynamic chord of about 1.2 million at the design Mach number. Six-component aerodynamic forces and moments were measured by an internal balance. Figure 27 shows a picture of the wind-tunnel model set in the tunnel.

In the winglet design phase, the aerodynamic drag was evaluated by Euler CFD analysis from an efficient design standpoint. Of course, the Euler CFD neglects the viscous effects and may lead to a misunderstanding of the actual design sensitivities. Therefore, a Navier–Stokes (NS) analysis was also conducted in addition to the Euler analysis for comparative use. For the NS analysis, an unstructured hybrid mesh [25] and a Spalart–Allmaras turbulence model [26] were applied. The meshes used for the NS analysis had approximately 1.3 million nodes for the baseline and 1.9 million nodes for the winglet configuration. For the drag evaluation of the NS analysis, the midfield drag decomposition method, the same as for the Euler analysis, was applied.

Table 1 Accuracy of the kriging model

		ΔCD, cts.	ΔBM, %
Designed	Kriging	−22.5	5.4
	CFD	−21.9	5.3
	Δ (CFD–kriging)	0.6	−0.1
Conventional	Kriging	−16.2	3.5
	CFD	−17.2	3.5
	Δ (CFD–kriging)	−1.0	0.0

Figure 28 shows a comparison of the drag reductions due to the winglet installation as an increment from the baseline (without winglet). The present design was validated by the good agreement of the Euler, NS, and the wind-tunnel test results.

The designed winglet was also tested in a low-speed wind tunnel to determine the low-speed aerodynamic characteristics. In the low-speed test, the improvement of the lift-to-drag ratio in the takeoff configuration and the absence of degradation of the maximum lift and pitch characteristics were validated.

V. Conclusions

In this paper, we report on a multidisciplinary design exploration for a winglet that was conducted for advanced winglet design in practical aircraft design.

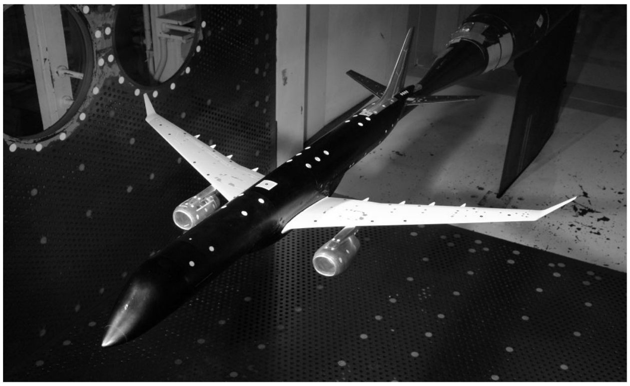

Fig. 27 Wind-tunnel model with designed winglet in the JAXA wind tunnel.

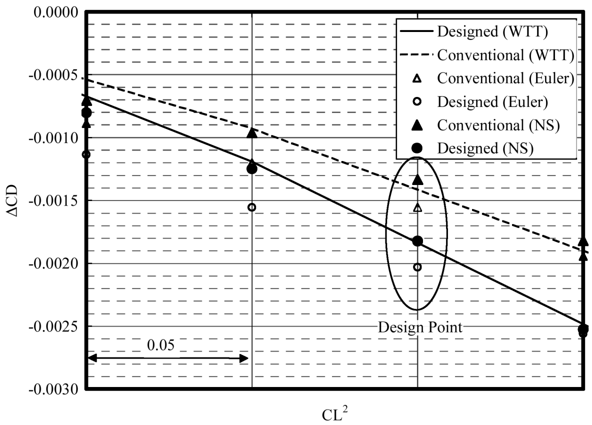

Fig. 28 Comparison of drag reductions due to the winglets.

[‡‡] Data available online at http://www.iat.jaxa.jp/res/wintec/0b00.html [retrieved 30 June 2008].

The minimization of block fuel and maximum takeoff weight were selected as design objectives. Both objectives were derived from CFD based aerodynamic drag and FEM based structural weight using various CFD and optimization techniques.

As for the CFD analysis, the midfield drag decomposition method and automatic mesh generation, which contributes to keeping mesh quality constant, were applied for accurate drag evaluation. Also, thanks to the parallel CFD computations, the design was completed within a day.

The aerodynamic and structural design information of the winglet configuration was obtained from the design exploration in the design space based on 32 sample individuals of winglet configuration using the kriging function approximation and its analysis of variance. In addition to the well-known effectiveness, such as the effectiveness of the winglet span length to induced drag and to bending moment, other important effectiveness such as that of the winglet cant angle to wave drag reduction was obtained.

The large cant angle of the winglet was found to be favorable for both the block fuel and maximum takeoff weight in the present study from the obtained the Pareto front.

Then, the practical design decision was explored by coupling the obtained design information with some design criteria, which were uncovered within the present numerical optimization. The decision based on the EI maximization was found to be very useful for the practical complex design problem.

Finally, the kriging function approximation, which was the foundation of the present design decision, was validated. Also, aerodynamic drag was validated by the wind-tunnel results. Therefore, the present design was validated.

Acknowledgments

The authors would like to express special thanks to S. Obayashi, S. Jeong of the Institute of Fluid Science at Tohoku University, and H. Morino of Mitsubishi Heavy Industries, Ltd. for their sincere cooperation in the present work. Also, we would like to express special thanks to Y. Ito of the University of Alabama at Birmingham for his cooperation in the automatic mesh generation tool development.

References

[1] Whitcomb, R. T., "A Design Approach and Selected Wind-Tunnel Results at High Subsonic Speeds for Wing-Tip Mounted Winglets," NASA TN D-8260, June 1976.

[2] Smith, S. C., "Trefftz-Plane Drag Minimization at Transonic Speeds," Society of Automotive Engineers Paper 971478, April 1997.

[3] Kroo, I., Nonplanar Wing Concepts for Increased Aircraft Efficiency, *VKI Lecture Series on Innovative Configurations and Advanced Concepts for Future Civil Aircraft*, The von Karman Institute for Fluid Dynamics, Belgium, June 2005.

[4] Kusunose, K., A Wake Integration Method for Airplane Drag Prediction, *The 21st Century COE Program International COE of Flow Dynamics Lecture Series*, Vol. 3, Tohoku Univ. Press, Sendai, Japan, 2005.

[5] Schmitt, V., and Destarac, D., "Recent Progress in Drag Prediction and Reduction for Civil Transport Aircraft at ONERA," AIAA Paper 98-0137, 1998.

[6] Yamazaki, W., Matsushima, K., and Nakahashi, K., "Application of Drag Decomposition Method to CFD Computational Results," AIAA Paper 2005-4723, 2005.

[7] Yamazaki, W., Matsushima, K., and Nakahashi, K., "Drag Prediction, Decomposition and Visualization in Unstructured Mesh CFD Solver of TAS-Code," *International Journal for Numerical Methods in Fluids*, Vol. 57, No. 4, 2008, pp. 417–436.
doi:10.1002/fld.1643

[8] Takenaka, K., Obayashi, S., Nakahashi, K., and Matsushima, K., "The Application of MDO Technologies to the Design of a High Performance Small Jet Aircraft—Lessons Learned and Some Practical Concerns," AIAA Paper 2005-4057, 2005.

[9] Oyama, A., Obayashi, S., Nakahashi, K., and Hirose, N.,"Aerodynamic Wing Optimization via Evolutionary Algorithms Based on Structured Coding," *Computational Fluid Dynamics Journal*, Vol. 8, No. 4, 2000, pp. 570–577.

[10] Kim, H. J., and Nakahashi, K., "Aerodynamic Design Optimization Using Unstructured Navier-Stokes Equations and Adjoint Method," International Council of the Aeronautical Sciences 2004-2.7.5, Sept. 2004.

[11] Jeong, S. J., Murayama, M., and Yamamoto, K., "Efficient Optimization Design Method Using Kriging Model," AIAA Paper 2004-0118, 2004.

[12] Mckay, M. D., Beckman, R. J., and Conover, W. J., "A Comparison of Three Methods for Selecting Values of Input Variables in the Analysis of Output from a Computer Code," *Technometrics*, Vol. 21, No. 2, 1979, pp. 239–245.
doi:10.2307/1268522

[13] Van Dam, C. P., Nikfetrat, K., Wong, K., and Vijgen, P. M. H. W., "Drag Prediction at Subsonic and Transonic Speeds Using Euler Methods," *Journal of Aircraft*, Vol. 32, No. 4, 1995, pp. 839–845.
doi:10.2514/3.46799

[14] Van Dam, C. P., and Nikfetrat, K., "Accurate Prediction of Drag Using Euler Methods," *Journal of Aircraft*, Vol. 29, No. 3, 1992, pp. 516–519.
doi:10.2514/3.46194

[15] Van Dam, C. P., "Recent Experience with Different Methods of Drag Prediction," *Progress in Aerospace Sciences*, Vol. 35, No. 8, 1999, pp. 751–798.
doi:10.1016/S0376-0421(99)00009-3

[16] Donald, R. J., Matthias, S., and William, J. W., "Efficient Global Optimization of Expensive Black-Box Function," *Journal of Global Optimization*, Vol. 13, No. 4, Dec. 1998, pp. 455–492.
doi:10.1023/A:1008306431147

[17] Matthias, S., William, J. W., and Donald, R. J., "Global Versus Local Search in Constrained Optimization of Computer Models," *New Developments and Applications in Experimental Design*, edited by N. Flournoy, W. F. Rosenberger, and W. K. Wong, Vol. 34, Institute of Mathematical Statistics, Hayward, CA, 1998, pp. 11–25.

[18] Obayashi, S., and Guruswamy, G. P., "Convergence Acceleration of an Aeroelastic Navier-Stokes Solver," *AIAA Journal*, Vol. 33, No. 6, 1995, pp. 1134–1141.
doi:10.2514/3.12533

[19] Venkatakrishnan, V., "On the Accuracy of Limiters and Convergence to Steady State Solutions," AIAA Paper 93-0880, 1993.

[20] Sharov, D., and Nakahashi, K., "Reordering of Hybrid Unstructured Grids for Lower-Upper Symmetric Gauss-Seidel Computations," *AIAA Journal*, Vol. 36, No. 3, 1998, pp. 484–486.

[21] Fujita, T., Koizumi, T., Kodera, M., Nakahashi, K., Iwamiya, T., and Nakamura, T., "Evaluation of Parallelized Unstructured-Grid CFD for Aircraft Applications," *Parallel Computational Fluid Dynamics: New Frontiers and Multi-Disciplinary Applications*, Elsevier, New York/Amsterdam, 2003, pp. 387–394.

[22] Ito, Y., and Nakahashi, K., "Direct Surface Triangulation Using Stereolithography Data," *AIAA Journal*, Vol. 40, No. 3, 2002, pp. 490–496.

[23] Sharov, D., and Nakahashi, K., "A Boundary Recovery Algorithm for Delaunay Tetrahedral Meshing," *Proceedings of the 5th International Conference on Numerical Grid Generation in Computational Field Simulations*, 1996, pp. 229–238.

[24] Koehler, J., and Owen, A., "Computer Experiments," *Handbook of Statistics, 13: Design and Analysis of Experiments*, edited by S. Ghosh and C. R. Rao, Elsevier, New York, 1996, pp. 261–308.

[25] Ito, Y., and Nakahashi, K., "Improvements in the Reliability and Quality of Unstructured Hybrid Mesh Generation,"*International Journal of Numerical Methods in Fluids*, Vol. 45, No. 1, 2004, pp. 79–108.
doi:10.1002/fld.669

[26] Spalart, P. R., and Allmaras, S. R., "A One-Equation Turbulence Model for Aerodynamic Flows," AIAA Paper 92-0439, Jan. 1992.